Supporting Information for:

Visualizing Reaction Pathways in Photoactive Yellow Protein from Nanoseconds to Seconds

Hyotcherl Ihee,[1,2][*][†] Sudarshan Rajagopal,[2][†] Vukica Šrajer,[3] Reinhard Pahl,[3] Spencer Anderson,[3] Marius Schmidt,[4] Friedrich Schotte,[5] Philip A. Anfinrud,[5] Michael Wulff,[6] Keith Moffat[2,3,7]

[1]Department of Chemistry and School of Molecular Science (BK21), Korea Advanced Institute of Science and Technology (KAIST), Daejeon 305-701, South Korea.
[2]Department of Biochemistry and Molecular Biology, University of Chicago, 920 East 58th Street, Chicago, IL 60637, USA.
[3]Center for Advanced Radiation Sources, University of Chicago, 920 East 58th Street, Chicago, IL 60637, USA.
[4]Physik-Department E17, Technische Universitaet Munchen, Garching, Germany.
[5]National Institutes of Health, Bethesda, MD 20982.
[6]European Synchrotron Radiation Facility, Grenoble Cedex 9, France.
[7]Institute for Biophysical Dynamics, University of Chicago, 920 East 58th Street, Chicago, IL 60637, USA.
[†]These authors contributed equally to the work.

*Corresponding author: Hyotcherl Ihee, Department of Chemistry, KAIST, 373-1 Guseong-dong, Yuseong-gu, Daejeon, 305-701, South Korea. Tel: +82-(0)42-869-2844, Fax: +82-(0)42-869-2810, email: hyotcherl.ihee@kaist.ac.kr

Data collection

In the presented time-resolved Laue crystallographic experiment, a chemical reaction in PYP crystals is triggered by a short laser pulse and X-ray pulses are used to probe structural changes at various time delays following reaction initiation. Data used in this study was collected over three synchrotron runs: two at BioCARS at the Advanced Photon Source (APS) and one at beamline ID09 at the European Synchrotron Radiation Facility (ESRF). Data collected at the ESRF covered the time range of 1 ns to 10 μs, while that collected at APS covered the time range of 6 μs to 1.33 s. In total, 47 time points from

1 ns to 1.33 s were used in the subsequent SVD analysis of the data (Fig. S1). The wavelength of the excitation laser was 485 nm and the pulse duration was typically several nanoseconds.

More specifically, APS data were collected using APS Undulator A at a 25 mm gap (first harmonic at 11.4 keV) in the standard operating mode of the APS storage ring. Laser pump pulses of 7 ns duration (fwhm) from a Nd:YAG pumped dye laser (Coumarin 480; 485nm) were used to illuminate the crystal from two sides to significantly increase the extent of photoactivation. Laser light was delivered to the sample via two separate optical fibers, with the total laser pulse energy of 1.3 ~ 1.7 mJ and the laser beam diameter at the sample of 0.6 and 0.9 mm for two fibers. The 6 μs duration of the probe X-ray pulses was determined by the opening time of the fast X-ray chopper running at 301.7 Hz. A single chopper opening at a given time delay following the laser pulse was selected by a ms shutter. Crystal temperature was maintained at 15 °C by an FTS crystal cooler. X-ray diffraction images were recorded on a MAR165 CCD detector by repeating the pump-probe sequence 15 times at 0.5 Hz and thus accumulating 15 X-ray exposures prior to the detector readout.

The ESRF data was collected on beamline ID9B at the ESRF. The X-rays were produced by a 236-pole in-vacuum undulator with a magnetic period of 17 mm. The undulator was operated with a 5.0 mm gap where the fundamental energy is 13.4 keV. The white beam was focused into a 0.10 x 0.06 mm^2 spot by a toroidal mirror with an energy-cut-off at 27 keV. The synchrotron was operated in 4-bunch mode, with 4 equidistant bunches separated by 705 ns. The bunch current was 10 mA and the pulse length 150 ps

(fwhm). Single pulses of X-rays were selected by a chopper rotating at 986.7 Hz, the 360th sub-harmonic of the orbit frequency. The chopper defined an open window of 500 ns centered on the selected pulse. Finally a pulsed millisecond shutter picked out a single pulse from the 986.7 Hz pulse train from the chopper. The Laue experiment was repeated quite slowly, at 0.5 Hz, due to the relatively long cycling time of PYP and the time it takes to cool the sample with a cold N_2 gas stream (15 °C). The sample excitation was done with the "Vibrant" nanosecond laser made by Quantel. This 10 Hz laser was synchronized to the RF clock and it produced 2.3 ns (fwhm) pulses with a jitter of 0.7 ns (rms). An OPO module converted the 1062 nm light from the fundamental to 485 nm with energy per pulse of ~ 2.5 mJ in the 1 mm^2 spot. The laser beam was brought to the sample in a 1 mm diameter fiber, which was connected to a focusing telescope. The laser beam was focused to a 0.5 mm diameter spot.

Time-resolved crystallographic data is four-dimensional; three traditional reciprocal space dimensions (hkl) and one additional dimension for the time delay. In previous experiments, an entire angular range was scanned at a fixed time delay and subsequently moved to another time delay. However this mode of data collection suffered from the systematic errors due to the inconsistent photoactivation between time points. To avoid this problem, time delay rather than the angular setting was the fast variable for all data sets collected in this work (1). That is, we collected data at all desired time points at one angular setting; advanced the angular setting to survey a different region of reciprocal space and repeat all time points; and continued in this way until the crystal no longer provides usable data. Normally, multiple crystals were used to obtain complete data in reciprocal space.

3

This method of data collection greatly minimizes systematic errors between time points and facilitates SVD analysis (2). A time series on a typical crystal consisted of a negative time point and four to six positive time points. The negative time point (-20 ns) allowed us to assess whether the protein had fully recovered the dark state after a cool-off time following each laser pulse, typically two seconds. To facilitate the comparison of the ESRF and APS data sets, the 10 μs time point was taken in all data sets.

Data processing

Statistics for individual dark and light data sets are shown in Table S1. All images from the APS runs were processed in LaueView (3, 4) including deconvolution (resulting in singles and multiples), with the exception of the G07 and G08 data sets. These two data sets and all ESRF data were processed in Precognition (Renz Research, *http://www.renzresearch.com/precognition*), a new program for Laue data analysis without deconvolution (resulting in singles only). The loss of multiples had only a small effect (less than 2%) on completeness as the data was collected with an undulator with quasi-monochromatic data. Time-resolved experiments yield structure factor amplitudes of the initial, dark state $|\mathbf{F}^{\mathbf{D}}(hkl)|$ and time-dependent structure factor amplitudes $|\mathbf{F}(hkl,t)|$. In our experiment, the structure factor amplitudes at a negative time point served as $|\mathbf{F}^{\mathbf{D}}(hkl)|$. From these amplitudes, time-dependent difference structure factor amplitudes $\Delta F(hkl,t) = |\mathbf{F}(hkl,t)| - |\mathbf{F}^{\mathbf{D}}(hkl)|$ are obtained for each time point t.

At this stage of the data reduction we have multiple, incomplete data sets of difference structure factor amplitudes from different crystals for each time point. These

4

data sets have to be combined to obtain one highly redundant and complete data set per time point. For this purpose, weighted averaging was carried out on individual values for $\Delta F(hkl,t)$ that correspond to the same time point. An averaged data set of $\Delta F(hkl,t)$ with a significantly enhanced signal to noise ratio (5) was obtained to 1.6 $\mathring{A}$ resolution for each time point (Table S1). Experimental, weighted difference electron density maps $\Delta\rho(t)$ were then generated by using weighted difference structure factor amplitudes, $w\Delta F(hkl,t)$, where w is a weighting factor to weight down observations with high experimental errors (6): w = $1 / (1 + \sigma^2/\langle\sigma^2\rangle)$. Phases were obtained from the dark (7, 8) PYP structure. This procedure is referred to as the difference Fourier approximation (9). Data statistics for averaged time-resolved Laue data sets are provided in Table S2.

Analysis by Singular Value Decomposition, the Basics

After data processing and averaging, we are left with a set of difference Fourier maps $\Delta\rho(t)$ as a function of time. In general, interpretation of such difference maps is not easy since they often suffer from a low signal to noise ratio arising from the difference Fourier approximation and experimental errors. In general, each difference density map, $\Delta\rho(t)$, consist of a mixture of difference density features arising from multiple intermediates contributing to the same time point. Separation of this mixture into the pure and time-independent difference electron densities of the intermediates is essential to determine the reaction mechanism and the structure of each intermediate. All three issues, (A) the differentiation of signal from noise, (B) the separation of intermediates and (C) the

5

determination of the kinetic mechanism can be resolved by a mathematical procedure called singular value decomposition (SVD) commonly used in the analysis of time-resolved spectroscopic data (10). Most notably, the SVD has been shown to work successfully with crystallographic data. Detailed information is reported in several references listed at the end of this manuscript (2, 11, 12).

Basically, SVD separates time- and real space-dependent data into only a few main spatial components and their time variations. The general steps involved in SVD are as follows. First, an M × N data matrix A is formed by arranging M grid points of $\Delta\rho(t)$ at N time points. SVD decomposes this time- and real space-dependent data matrix A into three matrices (13): left singular vectors (lSVs) in matrix U, each of which consists of an entire time-independent difference map; right singular vectors (rSVs) in matrix V^T, each of which contains the time dependence of the corresponding lSV; and the diagonal matrix S, whose diagonal elements, the singular values (SV), represent the degree to which their respective lSVs and rSVs contribute to the data matrix. In a mathematical form, $A = USV^T$, where V^T denotes the transpose of matrix V. Although N singular vectors result from the SVD, only a few of them contain signal. Selection of lSVs containing significant structural signal allows reconstitution of the data matrix $U'S'V'^T = A' \sim A$. In this reconstitution, vectors containing noises are excluded, thereby increasing the signal to noise ratio of the resulting matrix A' compared with the original matrix A. This procedure has been called SVD-flattening (2, 11, 12). In the present paper SVD-flattening was performed at the 3σ level with both the early and late data sets. Note that here the selection of significant singular vectors and values is greatly facilitated since the lSVs can be examined for features that

chemically and structurally make sense (see below), a property unique to time-resolved crystallography (10).

After the SVD was reapplied to matrix A' the procedure of rotation (13) was used to repartition signal that has spread to less significant singular vectors into significant ones. The significant rSVs are globally fit with a sum of exponentials. From this, relaxation times common to all rSVs can be determined. In later stages, the rSVs can be fit with different candidate mechanisms which reproduce the relaxation times according to $V' = CP$, where C is a matrix containing the concentrations of the intermediates based on a candidate mechanism and P is a set of linear parameters to bring the concentration to the scale of rSVs (13). The time-independent difference electron densities of the intermediates for this candidate mechanism, denoted by the matrix F, can then be extracted as follows:

Since
$$FC^T = A' = U'S'V'^T$$

$$= U'S'P^TC^T$$

then
$$F = U'S'P^T. \qquad (1)$$

Eqn. 1 can also be referred to as the projection of the lSVs onto the intermediate states.

Analysis by Singular Value Decomposition, Application to Data

When we attempted to perform SVD on the ESRF and APS data together, a discontinuity in rSV 2 was observed (Fig. S2), likely due to a significant increase in signal-to-noise in the APS data sets arising from increased photoactivation due to laser illumination from two sides of the crystal (14). Therefore, we proceeded to analyze the ESRF and APS data separately.

In the analysis of the ESRF data, SVD was individually performed on each time series (Table S1). From each of these analyses, rSV 1 was scaled to the others by a multiplicative factor to minimize deviation at the 10 μs time point, common to all crystals and time series. A clear trend was observable (Fig. S3A). After performing SVD on all of these early data sets together, quality factors (QFs) for the lSVs, a measure of their signal-to-noise level, were calculated (12). The QFs for the chromophore binding pocket are shown in black in Fig. S3B. Based on these QFs, singular vectors 2-6 were rotated, resulting in those shown in red in Fig. S3B. After rotation, only two significant singular vectors were identified, 1 and 2, as judged by the significant drop-off in QF between lSVs 2 and 3. Their corresponding rSVs were quite smooth and both were fit well by the same single exponential with a relaxation time of ~ 20 ns (Fig. S3C).

In the analysis of the APS data, without using any scale factors, the time series overlap well and show a clear trend in rSV 1 (Fig. S3D). After scaling the data together and calculating QFs for the chromophore binding pocket (black squares – Fig. S3E), it is clear that there are at least two significant singular vectors. However, it is difficult to assess whether there are any other significant ones because there is no sharp cutoff in QF. Based on the QFs, singular vectors 2-10 were rotated, with the results shown in red squares in Fig. 3E. This reveals clearly that there are three significant singular vectors and values. This is due to the rotation partitioning signal into singular vectors 2 and 3 at the expense of the singular vectors 4-10. lSVs 4-30 all have very low QFs and do not show significant signal and difference maps calculated from the insignificant singular vectors 4-30 show little-to-no signal (Fig. S4B). The three significant rSVs can be fit well by a sum of three

8

exponentials with relaxation times of 180 μs, 5 ms and 52 ms (Fig. S3F).

Fitting with a Chemical Kinetic Mechanism

The simplest mechanism which generates the single relaxation time (Fig. S3B) observed in the ESRF data is a two state system with an irreversible transition: α → β. The mechanism could be more complicated if the α or β states are heterogeneous or if there is reversibility. Reversibility is highly unlikely in the early stages of a photocycle, in which an initially highly strained chromophore thermally relaxes from high energy structures to low energy ones.

In the APS data, the data could be fully described by three singular vectors and values whose rSVs could readily be fit with three exponentials whose exponents are well separated in time (Fig. S3E). This suggests that the data could be fit with a simple sequential mechanism: β → γ → δ → dark state, where the β state must be consistent between the ESRF and APS data since they overlap in time in the 10 μs range. From these two mechanisms, we extracted the time-independent, species-associated difference electron densities (2).

Difference Refinement

Difference refinement was performed in SHELX-97 and the R-factors (R-free) for the refined structures were 35.6 (38.3) for I_{CP}, 37.0 (39.1) for pR_{CW} + pR_{E46Q}, 11.7 (11.6) for pB_1 and 18.1 (18.6) for pB_2. These R-factors are high compared to those seen in conventional static crystallographic refinement, which is likely due to the relatively lower

9

S/N of our difference data. Extrapolated maps (15) for these intermediates (Fig. S5 A-D) show good qualitative agreement and residual maps (ΔF_{calc} - ΔF_{obs}) (Fig. S4 E-H) show little difference density in the chromophore binding pocket. Chromophore binding pocket views of refined intermediate structures are shown in Fig. S6. The best measure of the quality of the intermediate structures and the candidate chemical kinetic models is in the posterior analysis (2), which show a good fit between our model and the data (see below).

To assess the quality of difference refinement, we compared the refined intermediate structures to the associated electron density extrapolated to 100% photoactivation ($F^{epol} = F^{calc} + e * \Delta F$, where e was adjusted to estimate for occupancy) (15). This comparison is shown for the chromophore in Figure S5A-D, which shows good correlation between features in the electron density map with the refined intermediate structures. We also calculated residual maps after the refinement of the four states, which are shown in Fig. S5E-H. For the α and β states, there are few features; features in the χ and δ states are likely due to the occupancy refinement, as the positive features are primarily on atoms which are already present in the refined model. However, the best way to assess the quality of these structures and candidate chemical kinetic mechanisms is posterior analysis, in which global analysis is used to fit the calculated to the experimental difference density.

Posterior Analysis

Difference electron density calculated from the structures of the refined intermediates (I_{CP}, pR_{CW} and pR_{E46Q} from the early analysis and pB_1 and pB_2 from the late

analysis (see below)) was used in posterior analysis, a process in which the experimental maps are fit with intermediate difference electron density using different candidate mechanisms (2). We chose the model shown in Fig. 4A (see paper) based on the initial constraints of the model, i.e., the number of intermediates and the number of relaxations, and simple kinetic reasoning. As the ESRF data could be fit well with an $\alpha \rightarrow \beta$ mechanism (where α corresponds to I_{CP} and β corresponds to pR_{CW} and pR_{E46Q}), the initial part of the mechanism allowed for parallel decays of I_{CP} to pR_{CW} and pR_{E46Q}. Similarly, we obtained a very good fit of the g state with the single intermediate pB_1, so pR_{CW} and pR_{E46Q} were allowed to decay to it in parallel. Based on the decline in total signal starting at ~ 10 ms (Figure S3F), it was likely that there was a significant pB_1 to dark state pathway along with the pB_1 to pB_2 transition, consistent with what has previously been observed in E46Q PYP (12). Fitting with this mechanism resulted in the rate coefficients shown in Fig. 4 legend (see paper).

To assess the quality of the model shown in Fig. 4A (see paper), we systematically set rate coefficients to 0 and then calculated the magnitude of the total squared deviation over all forty-seven time delays of features above $+3\sigma$ or below -3σ level in the experimental or calculated maps. The result of this analysis is shown in Fig. S7. Setting rate coefficients to 0 results in an increased deviation between the calculated and observed difference maps during the time range when the interconversion takes place. From this, we can conclude that our model indeed fits the data very well. However, we need to emphasize that this mechanisms is the simplest one that fits our data. Other mechanisms containing back reactions (16) cannot be ruled out since they would fit equally well and extract

structures identical to the ones observed here.

REFERENCES

1.   Ren, Z., Bourgeois, D., Helliwell, J., Moffat, K., Srajer, V. & Stoddard, B. (1999) *J. Synchr. Rad.* **6,** 891-917.

2.   Schmidt, M., Rajagopal, S., Ren, Z. & Moffat, K. (2003) *Biophys. J.* **84,** 2112-2129.

3.   Ren, Z. & Moffat, K. (1995) *J. Appl. Cryst.* **28,** 461-481.

4.   Ren, Z. & Moffat, K. (1995) *J. Appl. Cryst.* **28,** 482-493.

5.   Anderson, S., Srajer, V., Pahl, R., Rajagopal, S., Schotte, F., Anfinrud, P., Wulff, M. & Moffat, K. (2004) *Structure* **12,** 1039-1045.

6.   Ursby, T. & Bourgeois, D. (1997) *Acta Cryst. A* **53,** 564-575.

7.   Borgstahl, G. E., Williams, D. R. & Getzoff, E. D. (1995) *Biochemistry* **34,** 6278-6287.

8.   Anderson, S., Crosson, S. & Moffat, K. (2004) *Acta Cryst. D* **60,** 1008-1016.

9.   Henderson, R. & Moffat, J. K. (1971) *Acta Cryst. B* **B 27,** 1414-&.

10.   Golub, G. H. & Reinsch, C. (1970) *Numerische Mathematik* **14,** 403-&.

11.   Schmidt, M., Pahl, R., Srajer, V., Anderson, S., Ren, Z., Ihee, H., Rajagopal, S. & Moffat, K. (2004) *Proc. Natl. Acad. Sci.* **101,** 4799-4804.

12.   Rajagopal, S., Anderson, S., Srajer, V., Schmidt, M., Pahl, R. & Moffat, K. (2005) *Structure* **13,** 55-63.

13.   Henry, E. & Hofrichter, J. (1992) *Meth. Enzymol.* **210,** 129-192.

14.   Baxter, R. H., Ponomarenko, N., Srajer, V., Pahl, R., Moffat, K. & Norris, J. R. (2004) *Proc. Natl. Acad. Sci.* **101,** 5982-5987.

15.   Genick, U. K., Borgstahl, G. E., Ng, K., Ren, Z., Pradervand, C., Burke, P. M.,

Srajer, V., Teng, T. Y., Schildkamp, W., McRee, D. E., Moffat, K. & Getzoff, E. D. (1997) *Science* **275,** 1471-1475.

16.   Joshi, C. P., Borucki, B., Otto, H., Meyer, T. E., Cusanovich, M. A. & Heyn, M. (2005) *Biochemistry* **44,** 656-665.

FIGURE LEGENDS

Figure S1. The forty-seven time points from 1 ns to 1.33 s used in the SVD analysis (vertical lines near bottom of figure). The early data, from 1 ns to 10 µs, was collected at the ESRF; the late data, from 6 µs to 1.33 s, was collected at the APS (middle). Shown for comparison are the predicted spectroscopic species based on the room temperature photocycle (top).

Figure S2. Discontinuity in rSV 2 when applying SVD to the ESRF and APS data together. Adjustment of the scale factor between the ESRF and APS data sets resulted in continuity of rSV 1, but resulted in the discontinuity in rSV 2. This is likely due to a systematic difference in data quality between the two data sets.

Figure S3. Results of SVD analysis on the early (A-C) and late (D-F) data sets. (A) rSV 1 scaled to the 10 µs time point after separate SVD of all time series. (B) Chromophore QFs of lSVs before (black) and after (red) rotation (see text). (C) rSVs 1 (black) and 2 (red) after rotation. Shown are fits to a single exponential with $\tau \sim 20$ ns. (D) rSV 1 with no scale factor after SVD of all time series separately. (E) Chromophore QFs for the lSVs of the chromophore binding pocket before (black) and after (red) rotation. (F) Fits (shown in gray) of sums of three exponentials (180 µs, 5 ms and 52 ms) to the three significant right singular vectors.

Figure S4. (A) Maps reconstructed with singular vectors and values used in the analysis. Structural signal is limited to the chromophore binding pockets and other discrete regions of the protein. (B) Residual maps for the same time points. Note the near random distribution of electron density throughout the protein.

Figure S5. Chromophore binding pocket views of (A) I_{CP}, (B) a mixture of pR_{CW} and pR_{E46Q}, (C) pB_1 and (D) pB_2 with their associated extrapolated electron density simulating 100% photoactivation. Residual maps after refinement for the (E) α, (F) β, (G) χ, and (H) δ states. As discussed in the text, the α and β states were refined from the ESRF data and the χ and δ states from the APS data.

Figure S6. Chromophore binding pocket views of refined intermediate structures. Five distinct structural intermediates (I_{CP}, pR_{CW}, pR_{E46Q}, pB_1, and pB_2) were identified from four chemical states (α,β,γ and δ) shown in Fig. 2. The α, γ and δ states were modeled with single intermediate structures (I_{CP}, pB_1, and pB_2 respectively), while the β state required two intermediate structures to account for the observed difference electron density (pR_{CW} and pR_{E46Q}). Panel A, I_{CP}; Panel B, pR_{CW}; Panel C, pR_{E46Q}; Panel D, pB_1; and Panel E, pB_2. The dark state structure pG is in Panel F. The chromophore in each panel is colored differently for clarity.

Figure S7. Testing the quality of the mechanism proposed in Fig. 3 by setting certain rate coefficients to zero. A rate coefficient was set to zero and then all the other rate coefficients

16

were optimized; shown is the difference deviation from the original total squared deviation

for the mechanism shown in Fig. 4A (in the paper). (A) $k_5 = 0$. (B) $k_6 = 0$. (C) $k_2 = 0$. (D) k_2

$= 0$ and $k_6 = 0$. (E) $k_3 = 0$. (F) $k_3 = 0$ and $k_6 = 0$. (Original rate coefficients (s^{-1}): $k_1 = 4.76 \times$

10^7; $k_2 = 3.70 \times 10^7$; $k_3 = 3.03 \times 10^3$; $k_4 = 3.33 \times 10^4$; $k_5 = 55$; $k_6 = 100$; $k_7 = 7.1$.)

Fig. S1

Fig. S2

Fig. S3

A.

| 1 ns | 10 ns | 100 ns | 1 µs | 10 µs |

A. (*cont.*)

| 100 µs | 1 ms | 10 ms | 100 ms | 1 s |

Figure S4 (part 1)

B.

| 1 ns | 10 ns | 100 ns | 1 µs | 10 µs |

B. (*cont.*)

| 100 µs | 1 ms | 10 ms | 100 ms | 1 s |

Figure S4 (part 2)

Fig. S5

A I_{CP}

B pR_{CW}

C pR_{E46Q}

D pB_1

E pB_2

F pG
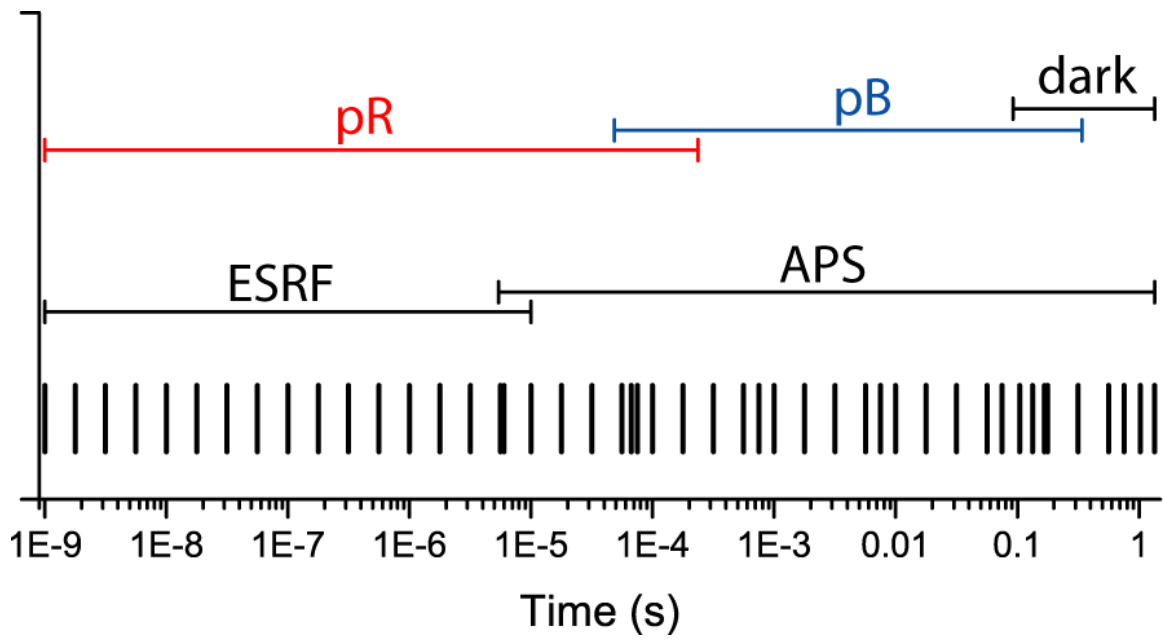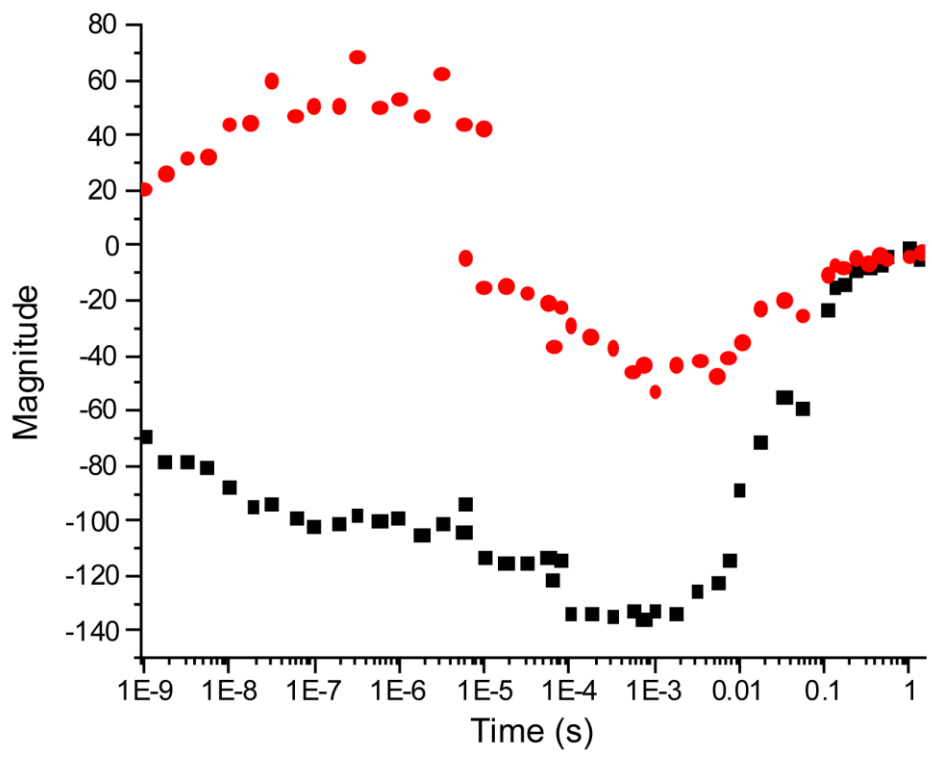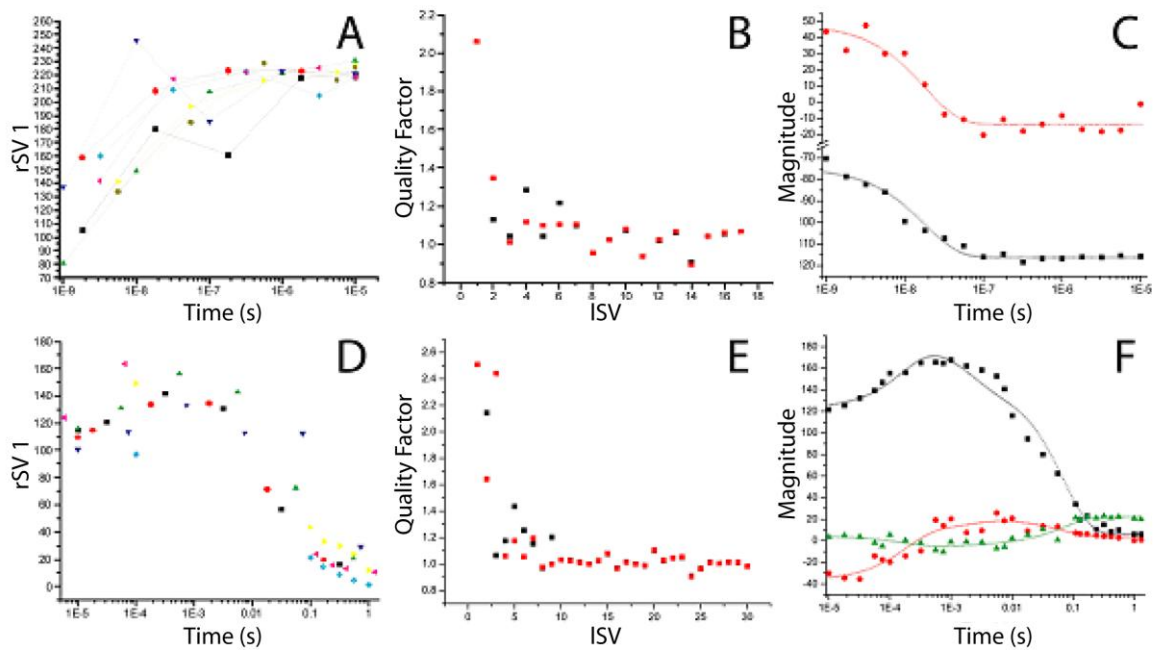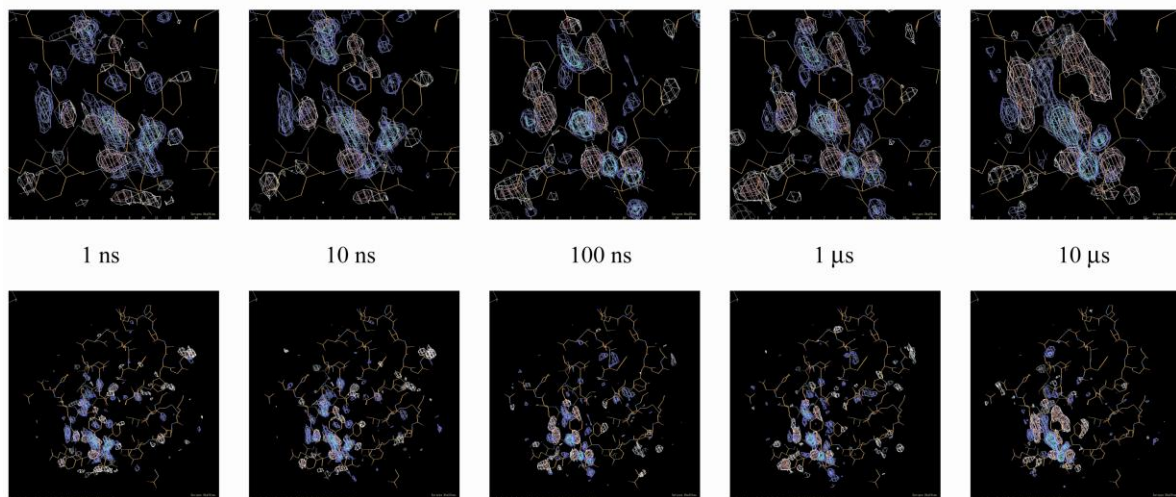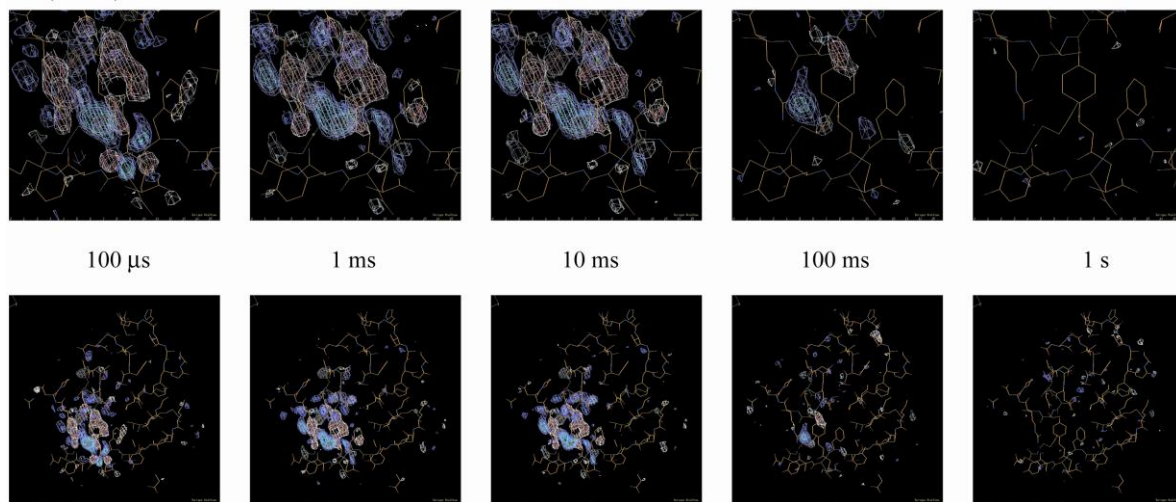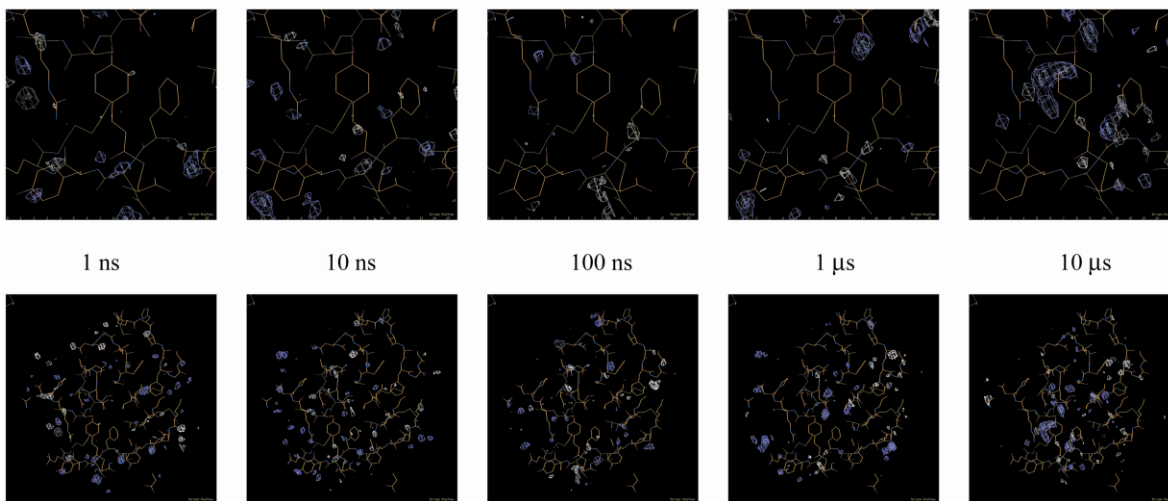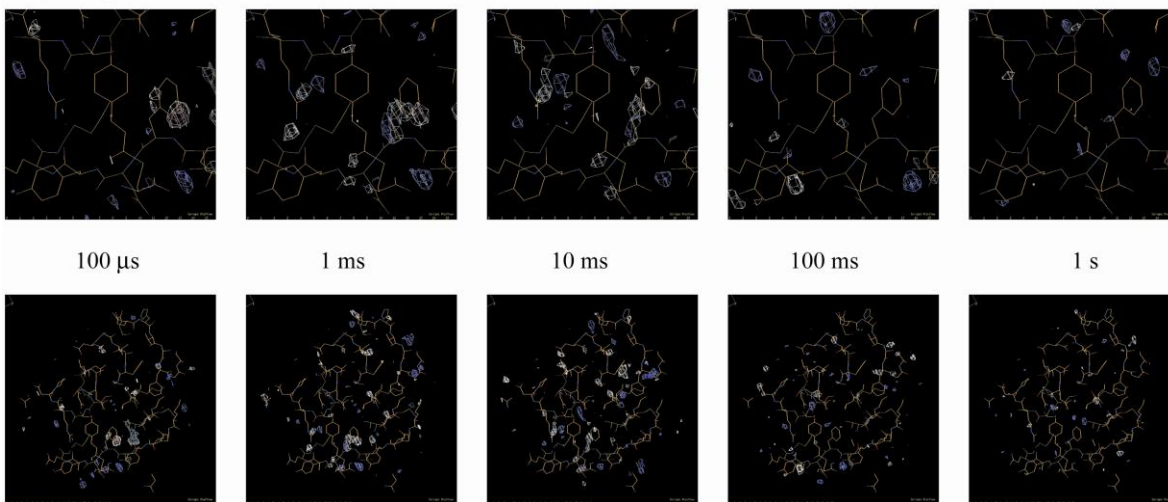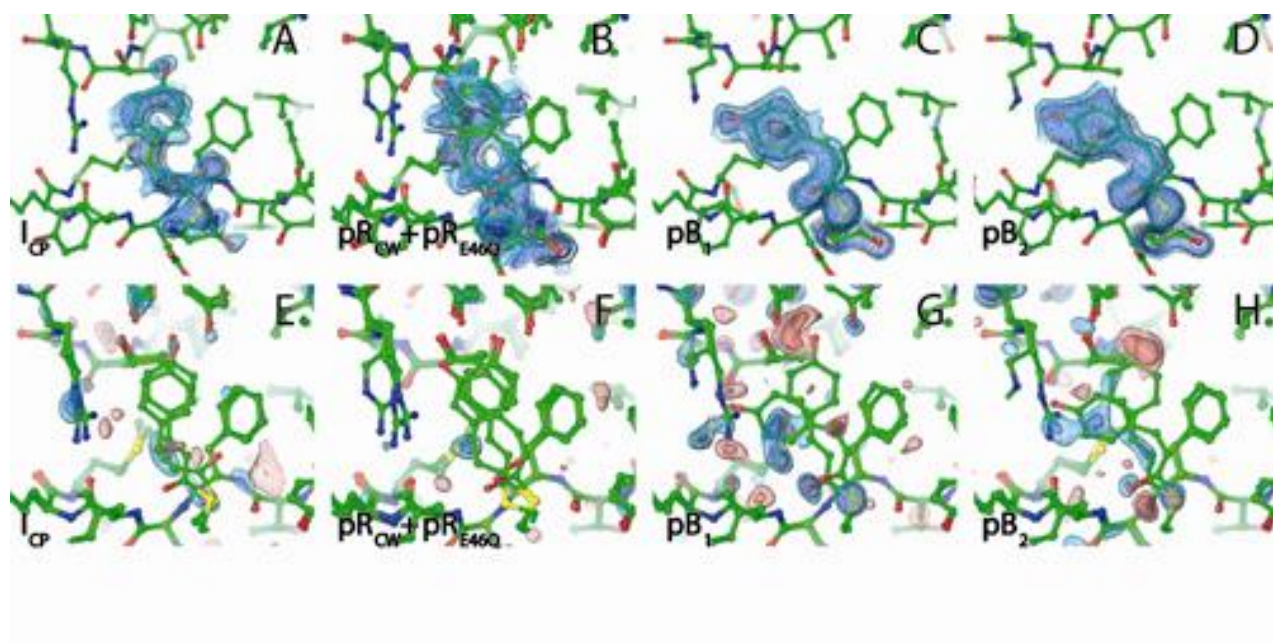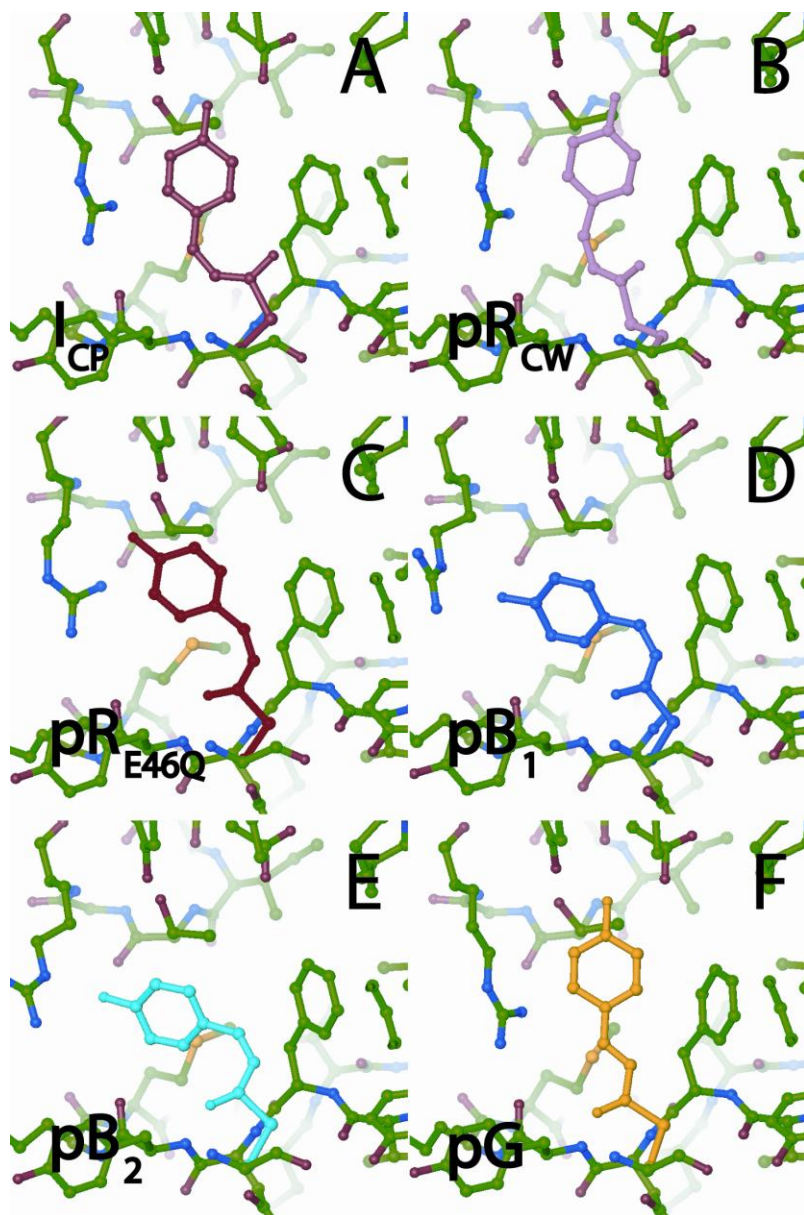
Fig. S6
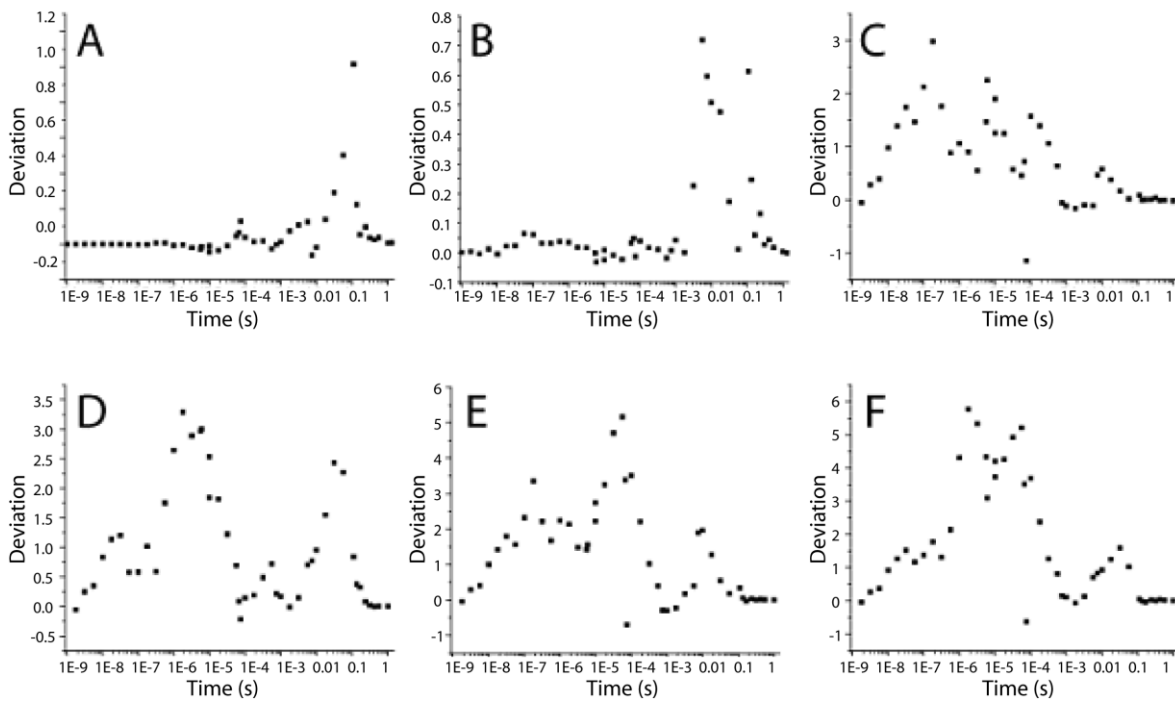
Fig. S7

Table S1. Data statistics for time-resolved Laue data sets. All ESRF0305 datasets and the G07/08 datasets from APS0304 were processed with Precognition without deconvolution (resulting in singles only); all other APS0304 datasets were processed with LaueView with deconvolution (resulting in singles and multiples). The loss of multiples had only a small effect (less than 2%) on completeness as the data was collected with an undulator with quasi-monochromatic data. Data with I/sig(I) less than 3 were rejected in the final stage so it is guaranteed that the best resolution shell has I/sig(I) better than 3.

Dataset Collection. *APS0212 run*: w, x, y and z; *APS0304 run*: A01, A02, A03, B01, B02, B03, C01, C02, D01, D02, D03, E01, E02, E03, E04, F01, F02, G04, G05, G06, G07 and G08; *ESRF0305 run*: 3ab, 3cd, 18ab, 24ab, 49ab, 49cd, 50ab, 50c, 50d, 50ef and 50gh.

Time delays. *aps0212*: -10 µs, 10 µs, 100 µs, 1 ms, 10 ms. *A*: -10 µs, 10 µs, 31.6 µs, 316 µs, 3.16 ms, 31.6 ms, 316 ms. *B*: -10 µs, 10 µs, 17.8 µs, 178 µs, 1.78 ms, 17.8 ms, 178 ms. *C*: -10 µs, 10 µs, 56.2 µs, 562 µs, 5.62 ms, 56.2 ms, 562 ms. *D*: -10 µs, 10 µs, 75 µs, 750 µs, 7.5 ms, 75 ms, 750 ms. *E*: -10 µs, 100 µs, 105 ms, 168 ms, 316 ms, 562 ms, 1 s. *F*: -10 µs, 6 µs, 66.5 µs, 133 ms, 237 ms, 421 ms, 1.33 s. *G*: -10 µs, 100 µs, 105 ms, 168 ms, 316 ms, 562 ms, 1s.

Shown for the APS0212 and APS0304 datasets are representative statistics from one time delay in the time series.

Table S1, continued.

Dataset identification	w	x	y	z
Time delays	aps0212	aps0212	aps0212	aps0212
Number of images	16	16	16	16
ϕ step (deg)	6	6	6	6
Singles and Multiples				
Observations	32066	28245	27689	27459
Unique Reflections	9412	8284	8589	8359
Redundancy	3.4	3.4	3.2	3.3
R_{merge} on F^2	10.82%	13.64%	11.36%	12.71%
R_{merge} on F	5.57%	6.23%	5.35%	6.61%
Completeness 30 to 1.60 Å	66.3%	57.3%	59.5%	56.9%
Completeness 1.66 to 1.60 Å	12.2%	4.9%	4.5%	1.3%

Table S1, continued.

Dataset identification	A01	A02	A03	B01	B02	B03	C01	C02
Time delays	A	A	A	B	B	B	C	C
Number of images	14	14	14	14	14	14	14	14
ϕ step (deg)	7	7	7	7	7	7	7	7
Singles and Multiples								
Observations	25396	22814	40279	23192	24028	38012	22453	36750
Unique Reflections	9358	8937	12513	8865	8950	12488	8746	12272
Redundancy	2.7	2.6	3.2	2.6	2.7	3.0	2.6	3.0
R_{merge} on F^2	9.53%	9.47%	7.52%	6.98%	6.66%	6.68%	8.09%	7.44%
R_{merge} on F	5.43%	5.10%	4.15%	3.57%	3.45%	3.77%	4.18%	4.00%
Completeness 30 to 1.60 Å	65.3%	61.1%	80.8%	57.5%	62.8%	81.5%	55.8%	80.2%
Completeness 1.66 to 1.60 Å	10.9%	6.8%	46.2%	3.6%	9.6%	48.0%	2.5%	44.9%

Table S1, continued.

Dataset identification	D01	D02	D03	E01	E02	E03	E04
Time delays	D	D	D	E	E	E	E
Number of images	14	14	14	14	14	14	14
ϕ step (deg)	7	7	7	7	7	7	7
Singles and Multiples							
Observations	21777	37103	37934	37501	38460	36634	37712
Unique Reflections	8464	12000	12271	12452	12450	12291	12222
Redundancy	2.6	3.1	3.1	3.0	3.1	3.0	3.1
R_{merge} on F^2	9.24%	6.86%	7.31%	7.69%	6.50%	6.03%	5.67%
R_{merge} on F	4.93%	3.81%	3.94%	3.20%	3.86%	3.57%	3.36%
Completeness 30 to 1.60 Å	58.8%	77.3%	78.5%	81.2%	81.5%	80.0%	79.8%
Completeness 1.66 to 1.60 Å	5.1%	43.2%	41.8%	47.3%	47.3%	48.2%	46.8%

Table S1, continued.

Dataset identification	F01	F02	G04	G05	G06	G07	G08
Time delays	F	F	G	G	G	G	G
Number of images	14	14	14	14	14	14	14
ϕ step (deg)	7	7	7	7	7	7	7
Singles and Multiples						*Singles*	
Observations	37744	34474	23502	23782	23533	35653	30699
Unique Reflections	12427	11978	9025	8889	8907	9626	9567
Redundancy	3.0	2.9	2.6	2.7	2.6	3.7	3.2
R_{merge} on F^2	6.85%	7.69%	6.59%	6.50%	9.53%	12.73%	13.00%
R_{merge} on F	3.73%	4.07%	3.45%	3.49%	3.89%	6.77%	6.92%
Completeness 30 to 1.60 Å	80.3%	77.8%	62.3%	59.9%	60.0%	63.1%	55.8%
Completeness 1.66 to 1.60 Å	43.0%	39.9%	6.7%	7.1%	7.8%	5.7%	2.2%

Table S1, continued.

Dataset identification	3ab	3ab	3ab	3ab	3ab	3ab	3cd	3cd	3cd
Time delay	-20 ns	1 ns	10 ns	100 ns	1 us	10 us	-20 ns	3.16 ns	31.6 ns
Number of images	32	32	32	32	32	32	32	32	32
ϕ step (deg)	5	5	5	5	5	5	5	5	5
Singles									
Observations	61790	62729	59497	57513	57872	57122	63047	62816	60049
Unique Reflections	12496	12578	12288	12162	12152	12174	13204	13125	12905
Redundancy	4.9	5.0	4.8	4.7	4.7	4.7	4.8	4.8	4.7
R_{merge} on F^2	8.80%	8.77%	9.53%	10.47%	10.55%	10.69%	8.98%	9.48%	10.13%
R_{merge} on F	5.06%	5.04%	9.99%	5.90%	5.94%	6.00%	5.06%	5.28%	5.67%
Completeness 30 to 1.50 Å	74.0%	74.5%	72.7%	72.1%	71.9%	72.1%	78.2%	77.8%	76.4%
Completeness 1.55 to 1.50 Å	36.7%	38.0%	35.6%	34.9%	35.8%	35.3%	42.4%	41.3%	40.7%

Table S1, continued.

Dataset identification	3cd	3cd	3cd	18ab	18ab	18ab	18ab	18ab	18ab
Time delay	316 ns	3.16 us	10 us	-20 ns	5.62 ns	56.2 ns	562 ns	5.62 us	10 us
Number of images	32	32	31	32	32	32	32	32	32
ϕ step (deg)	5	5	5	5	5	5	5	5	5
Singles									
Observations	60364	60232	57573	63217	61777	59043	59333	60040	59750
Unique Reflections	12993	13030	12871	13006	12861	12629	12649	12698	12695
Redundancy	4.7	4.6	4.5	4.9	4.8	4.7	4.7	4.7	4.7
R_{merge} on F^2	10.25%	10.38%	10.54%	9.05%	9.49%	10.06%	10.11%	9.93%	10.12%
R_{merge} on F	5.72%	5.75%	5.82%	5.15%	5.36%	5.66%	5.71%	5.62%	5.70%
Completeness 30 to 1.50 Å	76.9%	77.1%	76.2%	76.9%	76.2%	74.9%	74.9%	75.4%	75.4%
Completeness 1.55 to 1.50 Å	41.0%	40.6%	39.8%	38.8%	37.7%	35.3%	35.8%	35.6%	35.7%

Table S1, continued.

Dataset identification	24ab	24ab	24ab	49ab	49ab	49ab	49ab	49ab	49ab
Time delay	-20 ns	1 ns	10 us	-20 ns	1.78 ns	17.8 ns	178 ns	1.78 us	10 us
Number of images	65	65	65	32	32	32	32	32	32
ϕ step (deg)	5	5	5	5	5	5	5	5	5
Singles									
Observations	121309	121503	110246	65080	64795	61221	59713	60405	60188
Unique Reflections	13953	13918	13561	12946	12955	12683	12447	12602	12558
Redundancy	8.7	8.7	8.1	5.0	5.0	4.8	4.8	4.8	4.8
R_{merge} on F^2	10.63%	10.64%	12.20%	8.73%	8.80%	10.78%	11.32%	11.21%	11.42%
R_{merge} on F	5.93%	5.91%	6.67%	4.87%	4.91%	5.86%	6.11%	6.06%	6.17%
Completeness 30 to 1.50 Å	82.8%	82.6%	80.5%	76.8%	76.9%	75.3%	73.9%	74.8%	74.5%
Completeness 1.55 to 1.50 Å	55.0%	54.6%	50.7%	41.5%	39.8%	36.4%	35.9%	36.0%	35.3%

Table S1, continued.

Dataset identification	49cd	49cd	49cd	50ab	50ab	50ab	50ab	50c	50c
Time delay	-20 ns	1 ns	10 us	off	-20 ns	1 ns	10 us	-20 ns	1 ns
Number of images	66	66	65	66	66	66	66	16	16
ϕ step (deg)	5	5	5	5	5	5	5	5	5
Singles									
Observations	117265	118545	107482	133231	131557	131037	119975	32213	32398
Unique Reflections	14238	14281	13934	14490	14516	14434	14095	11013	10986
Redundancy	8.2	8.3	7.7	9.2	9.1	9.1	8.5	2.9	3.0
R_{merge} on F^2	13.85%	14.28%	14.28%	10.19%	10.21%	10.23%	11.97%	10.28%	10.35%
R_{merge} on F	7.15%	7.32%	7.37%	5.70%	5.74%	5.75%	6.52%	5.51%	5.55%
Completeness 30 to 1.50 Å	84.4%	84.7%	82.7%	86.0%	86.2%	85.7%	83.7%	65.4%	65.2%
Completeness 1.55 to 1.50 Å	60.3%	60.4%	56.9%	64.7%	64.6%	63.1%	58.6%	24.6%	24.1%

Table S1, continued.

Dataset identification	50c	50c	50c	50c	50d	50d	50d	50d	50d
Time delay	10 ns	100 ns	1 us	10 us	-20 ns	3.16 ns	31.6 ns	316 ns	3.16 us
Number of images	16	16	16	16	16	16	16	16	16
ϕ step (deg)	5	5	5	5	5	5	5	5	5
Singles									
Observations	31202	30612	30265	30441	32438	32313	31022	30912	31137
Unique Reflections	10736	10632	10574	10628	11098	11017	10749	10739	10785
Redundancy	2.9	2.9	2.9	2.9	2.9	2.9	2.9	2.9	2.9
R_{merge} on F^2	10.58%	11.17%	10.91%	10.98%	8.75%	8.79%	9.44%	9.61%	9.99%
R_{merge} on F	5.74%	6.01%	5.96%	5.99%	4.92%	4.96%	5.33%	5.40%	5.56%
Completeness 30 to 1.50 Å	63.7%	63.1%	62.8%	63.1%	65.9%	65.4%	63.8%	63.8%	64.0%
Completeness 1.55 to 1.50 Å	22.9%	22.3%	22.4%	22.6%	25.5%	23.6%	22.8%	22.5%	22.9%

Table S1, continued.

Dataset identification	50d	50ef	50ef	50ef	50ef	50ef	50ef	50gh	50gh
Time delay	10 us	-20 ns	5.62 ns	56.2 ns	562 ns	5.62 us	10 us	-20 ns	1.78 ns
Number of images	16	32	32	32	32	32	32	32	31
ϕ step (deg)	5	5	5	5	5	5	5	5	5
Singles									
Observations	31683	68485	67949	66580	66938	66861	67433	67317	64790
Unique Reflections	10811	13163	13124	13021	12981	13004	12984	13290	13201
Redundancy	2.9	5.2	5.2	5.1	5.2	5.1	5.2	5.1	4.9
R_{merge} on F^2	9.65%	8.05%	8.42%	8.74%	9.52%	9.84%	9.91%	8.62%	8.80%
R_{merge} on F	5.42%	4.42%	4.61%	4.82%	5.20%	9.80%	5.33%	4.70%	4.80%
Completeness 30 to 1.50 Å	64.2%	78.1%	77.9%	77.3%	77.0%	77.2%	77.0%	78.9%	78.3%
Completeness 1.55 to 1.50 Å	23.8%	41.6%	41.1%	41.4%	40.9%	40.7%	40.5%	41.1%	40.4%

Table S1, continued.

Dataset identification	50gh	50gh	50gh	50gh
Time delay	17.8 ns	178 ns	1.78 us	10 us
Number of images	32	32	32	32
ϕ step (deg)	5	5	5	5
Singles				
Observations	65363	64066	63991	64023
Unique Reflections	13064	13040	13008	13012
Redundancy	5.0	4.9	4.9	4.9
R_{merge} on F^2	8.96%	9.91%	11.08%	10.64%
R_{merge} on F	4.97%	5.43%	5.93%	5.74%
Completeness 30 to 1.50 Å	77.5%	77.4%	77.2%	77.2%
Completeness 1.55 to 1.50 Å	40.2%	40.2%	40.0%	39.1%

Table S2. Data statistics for averaged time-resolved Laue data sets.

Averaged Datasets	1 ns	1.78 ns	3.16 ns	5.62 ns	10 ns	17.8 ns	31.6 ns	56.2 ns
Total Observations	466212	129585	95129	129726	90699	126584	91071	125623
Unique Reflections	16251	15249	14406	15168	13421	15141	14066	15002
Redundancy	28.7	8.5	6.6	8.6	6.8	8.4	6.5	8.4
Completeness 30 to 1.50 Å	96.4%	86.8%	82.0%	86.8%	79.6%	86.2%	80.1%	85.9%
Completeness 1.55 to 1.50 Å	84.8%	54.6%	43.7%	52.5%	39.8%	53.4%	38.8%	49.8%
	100 ns	**178 ns**	**316 ns**	**562 ns**	**1 µs**	**1.78 µs**	**3.16 µs**	**5.62 µs**
Total Observations	88125	123779	91276	126271	88137	124396	91369	126901
Unique Reflections	13255	15056	14080	14932	13231	15008	13924	14933
Redundancy	6.6	8.2	6.5	8.5	6.7	8.3	6.6	8.5
Completeness 30 to 1.50 Å	78.7%	85.7%	80.2%	85.4%	78.5%	85.5%	79.3%	85.4%
Completeness 1.55 to 1.50 Å	38.4%	51.4%	36.8%	47.3%	37.9%	50.9%	34.2%	46.5%
	6 µs	**10 µs**	**17.8 µs**	**31.6 µs**	**56.2 µs**	**66.5 µs**	**75 µs**	**100 µs**
Total Observations	72218	1570807	85232	88489	59203	72554	96814	402935
Unique Reflections	13295	17325	13021	12945	12298	13357	13643	15667
Redundancy	5.4	90.7	6.5	6.8	4.8	5.4	7.1	25.7
Completeness 30 to 1.60 Å	88.8%	97.7%	88.3%	88.2%	83.8%	89.2%	90.8%	96.9%
Completeness 1.66 to 1.60 Å	61.6%	89.4%	53.1%	53.6%	46.8%	60.9%	64.8%	86.0%

Table S2, continued

Averaged Datasets	178 μs	316 μs	562 μs	750 μs	1 ms	1.78 ms	3.16 ms	5.62 ms
Total Observations	85245	88393	59203	96708	115459	85278	88324	59563
Unique Reflections	13023	12931	12319	13628	10873	13028	12921	12394
Redundancy	6.5	6.8	4.8	7.1	10.6	6.5	6.8	4.8
Completeness 30 to 1.60 Å	88.3%	88.1%	83.8%	90.7%	78.2%	88.3%	88.1%	84.1%
Completeness 1.66 to 1.60 Å	52.6%	52.5%	46.2%	64.9%	20.4%	52.5%	52.7%	48.2%

	7.5 ms	10 ms	17.8 ms	31.6 ms	56.2 ms	75 ms	105 ms	133 ms
Total Observations	96672	115459	85749	88277	59203	96750	288778	73010
Unique Reflections	13623	10856	13100	12914	12210	13634	15747	13441
Redundancy	7.1	10.6	6.5	6.8	4.8	7.1	18.3	5.4
Completeness 30 to 1.60 Å	90.9%	78.1%	88.6%	88.1%	83.2%	90.9%	96.9%	89.6%
Completeness 1.66 to 1.60 Å	65.4%	19.6%	54.6%	53.4%	45.1%	65.7%	87.4%	63.3%

	168 ms	178 ms	237 ms	316 ms	421 ms	562 ms	750 ms	1 s
Total Observations	288265	85323	73483	291840	72495	291841	96097	287476
Unique Reflections	15719	13035	13528	15914	13346	15914	13542	15676
Redundancy	18.3	6.5	5.3	18.3	5.4	18.3	7.1	18.3
Completeness 30 to 1.60 Å	96.8%	88.4%	90.1%	97.3%	89.3%	97.3%	90.5%	96.6%
Completeness 1.66 to 1.60 Å	86.4%	52.9%	64.5%	88.5%	61.3%	88.2%	63.9%	86.1%

Table S2, continued

Averaged Datasets	**1.33 s**
Total Observations	72223
Unique Reflections	13296
Redundancy	5.4
Completeness 30 to 1.60 Å	89.0%
Completeness 1.66 to 1.60 Å	60.2%